1-bit Mechanically Reconfigurable Metasurface as a Beam Splitter for Indoor Environments at 28 GHz

Marcos Baena-Molina, Ángel Palomares-Caballero, Ginés Martínez-García, Juan E. Galeote-Cazorla,
Alejandro Ramírez-Arroyo and Juan F. Valenzuela-Valdés

***Abstract*—This letter presents a mechanically reconfigurable metasurface (MRM) designed to operate in the n257 FR2 5G band with the ability to provide a reconfigurable beam splitting. The MRM unit cell consists of a metallic rod with a metallic cone-shaped element at its end. The actuator is an electromagnet that provides 1-bit reconfiguration by modifying the position of the cone-shaped element. A prototype is experimentally assessed. The measurements reveal a phase shift of $180^o \pm 30^o$ from 26.5 GHz to 29.5 GHz. Several beam configurations for the MRM have been measured where the scattering patterns show good agreement with the simulations. To demonstrate the potential of the proposed MRM, an indoor field trial has been performed. In a novel way, a simultaneously coverage of two different indoor zones has been achieved with an improvement of more than 10.9 dB of received average power.**

***Index Terms*—Reconfigurable metasurface, millimeter waves, beam splitting, mechanical reconfiguration.**

I. INTRODUCTION

THe growing demand for new electromagnetic (EM) devices to meet the requirements of next-generation wireless communications is undeniable [1]. One proposed solution is the reconfigurable intelligent surface (RIS) [2], which, placed in the propagation environment, controls the reflection of incoming waves to improve communication links [3]. As higher operating frequencies are adopted, the need for RIS becomes even more critical to overcome challenges like increased blockage losses [4].

RIS is similar to reconfigurable reflection metasurfaces, acting as a set of scatterers that locally control the phase of the incident wave. Various tuning mechanisms, such as PIN diodes, varactors, and liquid crystal materials, are commonly used [5]. However, mechanical reconfiguration, which has been less explored, offers a slower response but minimal electromagnetic impact since actuators are placed behind the reflection plane. Most designs operate below 10 GHz, with linear motion adjusting phase for linearly-polarized waves [6]–[9], or geometric phase shift for circularly-polarized waves [10]–[12]. For higher frequencies, such as those in 5G bands, a few works have explored mechanical reconfiguration, including a 1-bit design at 26 GHz using a rotating notched metal cylinder [13], and a 1-bit metasurface at 32 GHz with a double-gap ring [14]. Another design at 28 GHz uses expansion and compression of metastrips to control the reflected beam angle [15].

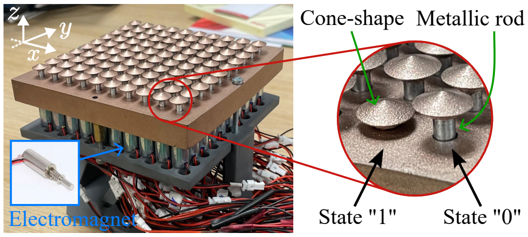

Fig. 1: MRM and the unit cell in its two states: OFF (“0”) and ON (“1”).

Field trials with RIS or reconfigurable metasurfaces are needed to assess their effectiveness in improving communication links in both outdoor [16] and indoor [17] environments. Indoor trials typically focus on non-line-of-sight (NLoS) scenarios, like L-shaped [8], [17], [18] or T-shaped corridors [19]. Most trials to date have been conducted in sub-6 GHz bands using diode-based metasurfaces.

In this letter, we present a cost-effective mechanically reconfigurable metasurface (MRM) design based on electromagnets that control the phase of each unit cell individually. The chosen operating band for the proposed design spans the entire n257 band of the FR2 5G spectrum. The proposed MRM is utilized to conduct a field trial in an indoor scenario at 28 GHz, which has not been previously characterized. The beam-splitting features are leveraged to enhance coverage simultaneously in two distinct areas within the same indoor scenario.

II. MECHANICALLY RECONFIGURABLE METASURFACE

The MRM prototype, shown in Fig. 1, consists of 10×10 unit cells. The zoomed view of Fig. 1 reveals the ON (“1”) and OFF (“0”) states, where the difference lies in the displacement of the metallic cone-shaped element perpendicular to the metasurface. Each unit cell state is set using an electromagnet actuator, also depicted in Fig. 1, which moves the metallic rod between two positions based on the supplied voltage. Due to the type of mechanical actuator, this imposes that the unit cell has a 1-bit capability. The switching speed between states for this type of actuator does not exceed tens of milliseconds. The rectilinear movement of the cone-shaped

This work has been supported by grant PID2020-112545RB-C54 funded by MCIN/AEI/10.13039/501100011033 and by the European Union NextGenerationEU/PRTR. It has also been supported by grants TED2021-129938B-I00, TED2021-131699B-I00 and PDC2023-145862-I00 funded by MCIN/AEI/10.13039/501100011033 and by the European Union NextGenerationEU/PRTR; and in part by the predoctoral grant FPU22/03392 *(Corresponding author: Marcos Baena-Molina)*.

Funding for open access charge: Universidad de Granada / CBUA.

M. Baena-Molina, Á. Palomares-Caballero, G. Martínez-García, J. E. Galeote-Cazorla and J. F. Valenzuela-Valdés are with the Department of Signal Theory, Telematics and Communications, Centre for Information and Communication Technologies (CITIC-UGR), University of Granada, 18071 Granada, Spain (email: marcosb@ugr.es, angelpc@ugr.es, gines.martinez@ugr.es, juane@ugr.es, juanvalenzuela@ugr.es).

A. Ramírez-Arroyo is with the Department of Electronic Systems, Aalborg University (AAU), 9220 Aalborg, Denmark (e-mail: araar@es.aau.dk).

element is 3 mm, defining the difference between its two positions. Each metallic rod is secured by holes in the main structure of the MRM to maintain stability during movement. The electromagnet also sets the periodicity between unit cells, determined by the 8 mm size of the electromagnet body in the x- and y-directions. Consequently, the periodicity between elements is set to 9 mm, allowing the cone-shaped elements to move without obstruction from neighboring unit cells. At 28 GHz, the periodicity and effective thickness (at OFF state) is $0.84\lambda_\mathrm{o}$ and $0.46\lambda_\mathrm{o}$, respectively. The effective thickness is from the metallic surface of the main structure of the MRM and the end of the cone-shaped element.

Fig. 2 shows the simulated E-field distributions at the center frequency for both states of the unit cell. The reflection phase is modified by 180º based on the position of the cone-shaped element relative to the metallic surface of the MRM. The E-field is the sum of incident and reflected EM waves. When the incident wave reaches the cone, part of the power is reflected, while the rest is transmitted to the rear, where it is reflected back by the metallic surface. The combination of the position of the cone-shaped element with the space it leaves behind provides the desired reflected phase difference. To prevent possible resonances on the rear of the mechanically moving element, we have chosen the cone shape. The frequencies of occurrence of these resonances depend on the electrical size of the rear part and the area between unit cells. As shown in [20], choosing a cone-shaped element shifts the unwanted resonance in the “0” state to higher frequencies. This paper focuses on experimentally validating the design and its application in a real scenario.

A. MRM fabrication

A key feature of the proposed MRM is its cost-effective manufacturing, achieved through stereolithography (SLA) 3-D printing for the cone-shaped elements and the structure housing the metallic rods. The Form 3 3-D printer from Formlabs is used, and the printed elements are metallized with a low-cost metallic spray (RS 247-4251 [21]) offering a conductivity of $\kappa \approx 10^4$ S/m. The skin depth is 31 μm at the lowest frequency and it is relevant when metallizing plastic pieces [22]. The reflection in the unit cell occurs due to a mismatch between free-space and the metallized cone. Performing an analysis similar to that in [23], it reveals that a metallization thickness of 50 μm ensures reflection losses under 0.2 dB. The approximate cost of each unit cell is €4.25. In addition, due to the simplicity of the control hardware, this alleviates the overall cost of the MRM.

B. Experimental validation of the MRM

To experimentally validate the fabricated MRM prototype, measurements have been conducted using a bi-static radar cross-section (RCS) setup shown in Fig. 3 (a). The system includes a 20-dBi transmitting horn antenna (Tx) and a receiving 20-dBi horn antenna (Rx), positioned slightly above Tx to avoid blockage. The antennas are placed about 1.45 m from the MRM to ensure plane-wave illumination. First, the reflected phase for each unit cell state is measured to calculate the phase shift between states. Two measurements are taken at normal incidence ($\theta = 0^\mathrm{o}$), with all unit cells in the MRM set to the same state for each measurement, simulating a periodic environment. The simulated and measured phase shift computed from both states of the unit cell is displayed in Fig. 3 (b). From 26.5 GHz to 29.5 GHz, the phase shift is between $180^\mathrm{o} \pm 30^\mathrm{o}$ demonstrating a 1-bit reconfiguration. A slight discrepancy is observed between the simulation and measurement. It is due to the actuator used, which is not capable of retracting all elements to the “1” state simultaneously, causing some of them not to be fully in that state. Fig. 3 (b) also presents the simulated magnitude of the unit cell for both states, which have been normalized to a metallic plate of equal size to the MRM. The average loss levels are 0.54 dB and 0.60 dB for for the ON state and OFF state, respectively. Through the following measurements, the level of losses of the unit cell will be determined experimentally. The next measurement for EM characterization involves determining the angular RCS gain for various MRM configurations. These configurations are measured by columns, meaning all unit cells in a column are set to the same state, simplifying the measurement as the illumination and reflections of the MRM occur in the same azimuth plane ($\phi = 0^\mathrm{o}$). Although each unit cell can also be configured individually, this measurement uses the setup in Fig. 3 (a), with the Rx antenna fixed and the Tx antenna rotating around the MRM. Fig. 4 (a)-4 (d) shows the phase distribution configured in the MRM for the measurements, quantized to 1-bit. Figs. 4 (e)-4 (g) display the scattering patterns for different configurations and frequencies, where each configuration deflects the incident wave in a specific angular direction (θ_o). The patterns are not normalized to allow for a quantitative comparison. The RCS gain is defined as follows:

$$\mathrm{G_{RCS}} = \sigma \frac{4\pi}{\lambda_\mathrm{o}^2}, \tag{1}$$

where σ represent the RCS of the MRM and λ_o is the operating wavelength. On one hand, the simulated results only

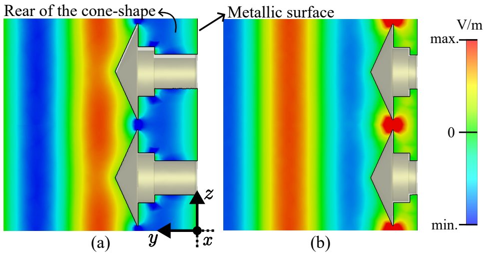

Fig. 2: E-field in the unit cell for the (a) OFF and (b) ON states at 28 GHz.

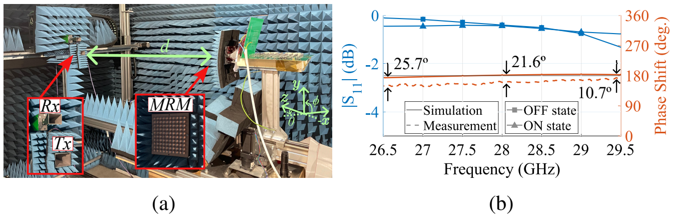

Fig. 3: (a) Setup to obtain the reflected phase behavior and the angular RCS gain. d = 1.45 m. (b) Magnitude and phase shift of the unit cell over frequency.

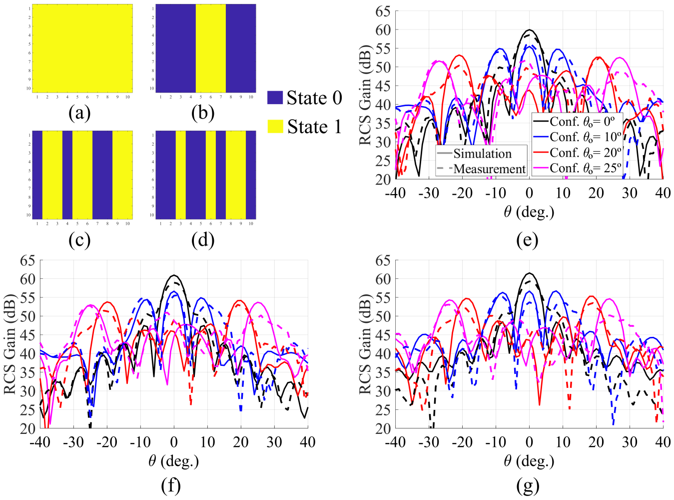

Fig. 4: Phase distribution for reflection in the MRM at XY plane ($\phi = 0^{\mathrm{o}}$) with (a) $\theta_{\mathrm{o}} = 0^{\mathrm{o}}$, (b) $\theta_{\mathrm{o}} = 10^{\mathrm{o}}$, (c) $\theta_{\mathrm{o}} = 20^{\mathrm{o}}$ y (d) $\theta_{\mathrm{o}} = 25^{\mathrm{o}}$. Measurement of the angular-depending RCS gain at (e) 26.5 GHz, (f) 28 GHz and (g) 29.5 GHz.

provide the σ of the MRM so, applying (1), G_{RCS} is obtained. On the other hand, σ cannot be measured directly and the following link budget must be applied to obtain it:

$$\mathrm{G}_{\mathrm{RCS}}^{\mathrm{mea.}} = -\mathrm{P}_t + \mathrm{P}_r - \mathrm{G}_{Tx} - \mathrm{G}_{Rx} - \mathrm{PG}_1 - \mathrm{PG}_2 + \mathrm{L}, \quad (2)$$

where P_t and P_r represent the transmitted power by the Tx antenna and the power measured at the Rx antenna, respectively. G_{Rx} and G_{Tx} indicate the gain on the Rx and Tx antennas. On the other hand, PG_1 and PG_2 represent the path-gains associated with propagation in the Tx-MRM and MRM-Rx paths, respectively, whereas L corresponds to the losses associated with the cables used. In Figs. 4 (e)-4 (g), a good agreement between simulations and measurements can be seen for the selected MRM configurations. For all measured configurations and frequencies there is an average difference of 1.87 dB. It is important to note that this difference is the combined measured losses for the ON and OFF states in the unit cell. This is an increase of about 1.20 dB with respect to the simulated losses. Based on simulated results, the scanning range of the proposed MRM can be extended up to 40º. The impact of tolerances in the electromagnet movement has also been studied through simulations. They produce a negligible effect in the performance and confirm the robustness of the MRM design. For the oblique incidence performance, we have found that the MRM supports reciprocity. That is, a simulated RCS gain of around 55 dB is obtained in $\theta = 0^{\mathrm{o}}$ for all θ_{o} shown in Fig. 4. In this oblique incidence situation, beam splitting and specular lobes are also present. Since the metasurface is 1-bit and illuminated by a plane wave, both the desired and quantization beams are generated [24]. Consequently, the MRM effectively divides the power between two angular directions with minimal effort. This capability can be utilized in practical situations where coverage is needed in two separate areas simultaneously. Nevertheless, the proposed 1-bit MRM is not limited to beam splitting and can generate a single beam (considering near field feeding) or multiple beams.

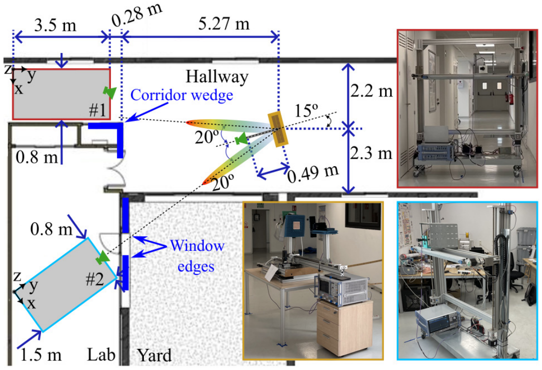

Fig. 5: Scenario scheme for the MRM in a beam splitting configuration of 20º. Region #1 corresponds with a corridor and region #2 with a laboratory room. Diffraction sources modeled with UTD are highlighted in blue.

III. BEAM SPLITTING USE CASE SCENARIO

The MRM has been tested in an indoor scenario to showcase its beam-splitting capabilities. It has been employed a vector network analyzer (VNA) R&S-ZVA67 in continuous wave (CW) mode at 28 GHz with $\mathrm{P}_t = 20\,\mathrm{dBm}$ on the Tx side and a signal spectrum analyzer (R&S FSW50) on the Rx side. Tx and Rx antennas are those used in the previous section. A scheme of the experimental setup is illustrated in Fig. 5. The MRM is located strategically in a hallway, aiming for beam-splitting capabilities. Given an optimal θ_{o} choice, the MRM is expected to cover both shadowed regions #1 and #2, i.e., a corridor and a laboratory room, respectively. Therefore, both regions are scanned through a rectangular array lying on the XY axes at a height $z = 1.6$ m. At region #1, the array dimensions are $3.5\text{ m} \times 0.8\text{ m}$ with 8×21 elements; whereas at region #2 these are $1.5\text{ m} \times 0.8\text{ m}$ with 6×21 elements. Each scan considers output angles of 0º, 10º, 20º, and 25º for the MRM, with Rx antennas aligned accordingly. The $\theta_o = 20^{\mathrm{o}}$ case is optimal, covering both regions simultaneously. To compare, the experimental setup has been simulated, and the full link budget (as shown in 2) has been calculated between Tx and each Rx position under free-space conditions to estimate the received power (P_r). A correction based on the uniform theory of diffraction (UTD) has been applied to account for shadowing effects from the corner in region #1 and window edges in region #2 [25].

The simulated and measured P_r for regions #1 and #2 are presented in Figs. 6 and 7, respectively. Although there may be slight differences between simulation and experimentation due to the uncertainty of location of the elements, the illuminated areas between the two cases match. Focusing on Fig. 6, i.e., region #1, simulations based on UTD are similar to the measurements. Specifically, for $\theta_{\mathrm{o}} = 25^{\mathrm{o}}$, it can be seen that all the corridor is covered except for the lower-right side where the corner produces a shadow region. For $\theta_{\mathrm{o}} = 20^{\mathrm{o}}$, the maximum power is focused on the right side in both simulation and measurement, corresponding with the MRM beam spatial location [see Fig. 4 (f)]. In contrast, for the angles $\theta_{\mathrm{o}} = 0^{\mathrm{o}}$ and $\theta_{\mathrm{o}} = 10^{\mathrm{o}}$, the received power is significantly lower since the EM wave reaches the desired region from side lobes of the MRM. On the other hand, Fig. 7 shows

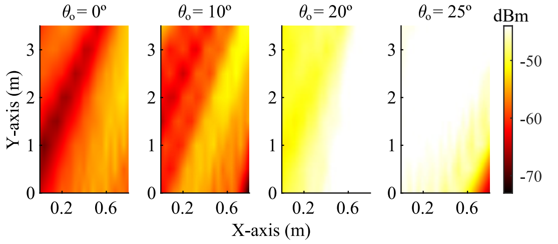

(a) Simulation.

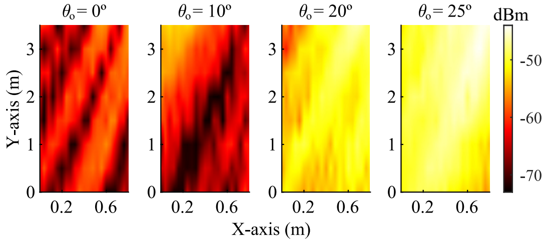

(b) Measurements.

Fig. 6: Simulated and measured received power at region #1 (corridor) for the different MRM configurations.

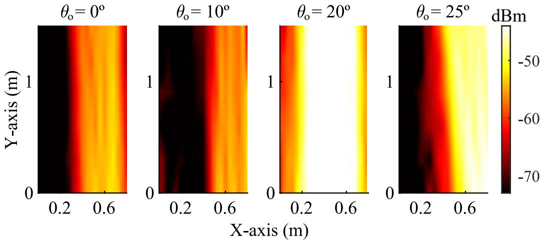

(a) Simulation.

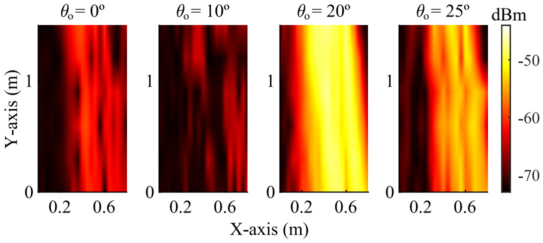

(b) Measurements.

Fig. 7: Simulated and measured received power at region #2 (laboratory room) for the different MRM configurations.

TABLE I: Comparison table of MRM in the literature.

	[8]	[11]	[14]	[15]	**This work**
Freq. (GHz)	2.55	6-7.4	32	27.5-28.5	**26.5-29.5**
No. elements	4 x 4	20 x 20	28 x 14	40 x 40	**10 x 10**
Array size (λ_o)	4.35 x 4.35	19.43 x 19.43	12.8 x 12.8	13.53* x 9.33	**8.4 x 8.4**
Min. Reconfig.	Subarray	Subarray	Column	Array	**Unit cell**
Meas. Scanning (°)	±13 - ±27	n. a.	±10 - ±40	±15 - ±32§	**0 - ±25**
Polarization†	VP-HP	CP	HP	VP-HP	**VP-HP**
Power cons.‡(W)	n. a.	9.5e-5	8.9e-3	8.4e-3	**0.45**
Field trial	Yes	No	Yes	No	**Yes**
Average P_r enhancement (dB)	5.2	n. a.	8	n. a.	$>$ **10.9**

* The dimension in the X direction varies between 9.33 and 17.73 λ_o.
† VP, HP and CP stand for vertical, horizontal and circular polarizations.
§ Continuous scanning. ‡ At unit cell level.

the results obtained for the region #2, which also illustrates the agreement between simulations and measurements (see shadowed areas on Fig. 7). For $\theta_o = 0°$ and $\theta_o = 10°$, MRM side lobes are attenuated by the left edge of the window (see Fig. 4), which produces the observed rectangular shadowed regions. For $\theta_o = 20°$, as aforementioned, it is obtained the maximum coverage observing the MRM output beam centered at the region #2. Finally, for $\theta_o = 25°$, the beam appears more inclined compared to $\theta_o = 20°$. Considering both regions as a single scenario given the beam splitting capabilities, the P_r for $\theta_o = 20°$ coverages the setup with $\mathrm{P}_r > -50\,\mathrm{dBm}$ at most of the Rx locations. On the other hand, for $\theta_o \neq 20°$, i.e., a non-optimal MRM configuration, P_r might not be high enough to provide coverage on one of the regions. Specifically, for the MRM configuration $\theta_o = 0°$ (analogous to a metallic plate), the average P_r over the entire measurement area is -63.1 dBm and -67.0 dBm in regions #1 and #2, respectively. The maximum value measured in region #1 is -55.5 dBm while in region #2 the maximum is -59.1 dBm. On the other hand for MRM configuration $\theta_o = 20°$, the average P_r is -51.7 dBm and -56.1 dBm, and the maximum value obtained is -46.3 dBm and -46.9 dBm, in region #1 and #2, respectively. The results presented in this section highlight the benefits of an optimal MRM configuration to provide coverage across two different areas simultaneously. Considering the received power at the regions covered by the MRM, the Signal-to-Noise Ratio (SNR) is between 20 dB and 26 dB; making the proposed design suitable for the n257 FR2 5G communication.

Finally, a comparison with other MRM found in the literature is summarized in Table I. The proposed MRM stands out for its operating frequency and bandwidth outperforming other works with either lower frequency (e.g., [8], [11]) or narrower bandwidth (e.g., [14], [15]). It also demonstrates effectiveness in field trials, boosting received power in the 5G n257 band. While [8] also conducted a field trial at 2.55 GHz, the beam-splitting advantage of a 1-bit MRM was not explored nor characterized in [8] or [14]. Therefore, for the first time, the benefit of beam-splitting in improving indoor coverage from an MRM in this frequency band has been presented demonstrating an average improvement of more than 10.9 dB. The switching speed of the proposed MRM is similar to the compared MRMs, which use different type of mechanical actuators. The increased power consumption of the MRM helps reduce the complexity of the control software and hardware. This can be improved by using alternative actuators without modifying the presented unit cell design.

IV. CONCLUSION

It is presented a mechanically reconfigurable beam splitter metasurface that provides coverage enhancement in the n257 FR2 5G band. Due to its 1-bit reconfiguration capability, the reflection of the incident wave is split into two main beams enabling simultaneously coverage in two regions. A field trial in an indoor scenario has been carried out using the proposed MRM. At 28 GHz, the best configuration improves the average received power from 10.9 dB up to a maximum of 20.0 dB. Based on its switching speed, this MRM is suitable for dynamically filling coverage holes with changes in quasi-static scenarios above the second.

REFERENCES

[1] W. Saad, M. Bennis and M. Chen, “A Vision of 6G Wireless Systems: Applications, Trends, Technologies, and Open Research Problems,” *IEEE Netw.*, vol. 34, no. 3, pp. 134-142, May/June 2020.

[2] M. Matthaiou, O. Yurduseven, H. Q. Ngo, D. Morales-Jimenez, S. L. Cotton and V. F. Fusco, “The Road to 6G: Ten Physical Layer Challenges for Communications Engineers,” *IEEE Commun. Mag.*, vol. 59, no. 1, pp. 64-69, January 2021.

[3] Q. Wu and R. Zhang, “Towards Smart and Reconfigurable Environment: Intelligent Reflecting Surface Aided Wireless Network,” *IEEE Commun. Mag.*, vol. 58, no. 1, pp. 106-112, January 2020.

[4] M. Shafi *et al.*, “Microwave vs. Millimeter-Wave Propagation Channels: Key Differences and Impact on 5G Cellular Systems,” *IEEE Commun. Mag.*, vol. 56, no. 12, pp. 14-20, December 2018.

[5] B. Rana, S. -S. Cho and I. -P. Hong, “Review Paper on Hardware of Reconfigurable Intelligent Surfaces,” *IEEE Access*, vol. 11, pp. 29614-29634, 2023.

[6] X. Yang *et al.*, “A Mechanically Reconfigurable Reflectarray With Slotted Patches of Tunable Height,” *IEEE Antennas Wirel. Propag. Lett.*, vol. 17, no. 4, pp. 555-558, April 2018.

[7] S. M. A. Momeni Hasan Abadi, J. H. Booske, and N. Behdad, “MAcro-electro-mechanical systems (MÆMS) based concept for microwave beam steering in reflectarray antennas,” *J. Appl. Phys.*, vol. 120, no. 5, Aug. 2016, Art. no. 054901.

[8] K. Qu *et al.*, “An electromechanically reconfigurable intelligent surface for enhancing Sub-6G wireless communication signal,” *Journal of Information and Intelligence*, vol. 1, no 3, p. 207-216, Sept. 2023.

[9] L. Lu, C. Liu, X. Liu and Y. Huang, “A Mechanical Reconfigurable Reflectarray Based on Magnetic Force Tuning,” *IEEE Antennas Wirel. Propag. Lett.*, vol. 23, no. 2, pp. 528-532, Feb. 2024.

[10] X. Yang *et al.*, “A Broadband High-Efficiency Reconfigurable Reflectarray Antenna Using Mechanically Rotational Elements,” *IEEE Trans. Antennas Propag.*, vol. 65, no. 8, pp. 3959-3966, Aug. 2017.

[11] Q. Xu *et al.*, “Mechanically reprogrammable Pancharatnam–Berry metasurface for microwaves,” *Adv. Photon.*, vol. 4, no. 1, Feb. 2022, Art. no. 016002.

[12] S. Bi, L. Xu, X. Cheng, Y. Sun, Q. Zhang and C. Yuan, “An All-Metal, Simple-Structured Reflectarray Antenna With 2-D Beam-Steerable Capability,” *IEEE Antennas Wirel. Propag. Lett.*, vol. 22, no. 1, pp. 129-133, Jan. 2023.

[13] P. Mei, S. Zhang and G. F. Pedersen, “A Low-Cost, High-Efficiency and Full-Metal Reflectarray Antenna With Mechanically 2-D Beam-Steerable Capabilities for 5G Applications,” *IEEE Trans. Antennas Propag.*, vol. 68, no. 10, pp. 6997-7006, Oct. 2020.

[14] H. Jeong, E. Park, R. Phon, and S. Lim, “Mechatronic reconfigurable intelligent-surface-driven indoor fifth-generation wireless communication,” *Adv. Intell. Syst.*, vol. 4, no. 12, Dec. 2022, Art. no. 2200185.

[15] S. Kiv, R. Phon, and S. Lim, “Power screw-assisted reconfigurable reflective metasurface with spatial modulation,” *Int. J. Mech. Sci.*, vol. 274, no. 109245, July 2024.

[16] X. Pei *et al.*, “RIS-Aided Wireless Communications: Prototyping, Adaptive Beamforming, and Indoor/Outdoor Field Trials,”*IEEE Trans. Commun.*, vol. 69, no. 12, pp. 8627-8640, Dec. 2021.

[17] J. Rains *et al.*, “High-Resolution Programmable Scattering for Wireless Coverage Enhancement: An Indoor Field Trial Campaign,” *IEEE Trans. Antennas and Propagation*, vol. 71, no. 1, pp. 518-530, Jan. 2023.

[18] Y. Li *et al.*, “Path Loss Modeling for the RIS-Assisted Channel in a Corridor Scenario in mmWave Bands,” in *2022 IEEE Globecom Workshops (GC Wkshps)*, Rio de Janeiro, Brazil, 2022, pp. 1478-1483.

[19] H. Xue *et al.*, “A Reconfigurable Metasurface Enhancing Signal Coverage for Wireless Communication Using Reduced Numbers of p-i-n Diodes,” *IEEE Trans. Microw. Theory Techn.*, vol. 72, no. 3, pp. 1964-1978, March 2024.

[20] M. Baena-Molina, Á. Palomares-Caballero, G. Martínez-García, R. Padial-Allué, P. Padilla and J. F. Valenzuela-Valdés, “1-bit RIS Unit Cell with Mechanical Reconfiguration at 28 GHz,” in *2024 18th European Conference on Antennas and Propagation (EuCAP)*, Glasgow, United Kingdom, 2024.

[21] *RS 247-4251 Aerosol DataSheet. Silver Coated Copper Screening Compound*. Accessed: Nov., 2024. [Online]. Available: https://docs.rs-online.com/16c4/0900766b8158361e.pdf

[22] A. Tamayo-Dominguez, J. -M. Fernandez-Gonzalez and M. Sierra-Perez, “Metal-Coated 3D-Printed Waveguide Devices for mm-Wave Applications [Application Notes],” *IEEE Microw. Mag.*, vol. 20, no. 9, pp. 18-31, Sept. 2019.

[23] A. Roehrner, G. Strauss and T. Eibert, “A broadband inhomogeneous frequency selective surface on quartz glass substrate,” in *2022 16th European Conference on Antennas and Propagation (EuCAP)*, Madrid, Spain, 2022.

[24] T. J. Cui, M. Q. Qi, X. Wan, J. Zhao, and Q. Cheng, “Coding metamaterials, digital metamaterials and programmable metamaterials,” *Light, Sci. Appl.*, vol. 3, no. 10, p. e218, Oct. 2014.

[25] R. G. Kouyoumjian and P. H. Pathak, “A uniform geometrical theory of diffraction for an edge in a perfectly conducting surface,” *Proc. IEEE*, vol. 62, no. 11, pp. 1448-1461, 1974.